Multispectral imaging of tissue absorption and scattering using spatial frequency domain imaging and a computed-tomography imaging spectrometer

Jessie R. Weber,[a,][*] David J. Cuccia,[b] William R. Johnson,[c] Gregory H. Bearman,[d] Anthony J. Durkin,[a] Mike Hsu,[e] Alexander Lin,[e] Devin K. Binder,[e] Dan Wilson,[c] and Bruce J. Tromberg[a]
[a]University of California, Irvine, Beckman Laser Institute and Medical Clinic, 1002 Health Sciences Road East, Irvine, California, 92612
[b]Modulated Imaging, Inc., 1002 Health Sciences Road East, Irvine, California 92612
[c]California Institute of Technology, Jet Propulsion Laboratory, 4800 Oak Grove Road, Pasadena, California 91109
[d]Snapshot Spectra, Inc., 974 East Elizabeth, Pasadena, California 91104
[e]University of California, Riverside, Center for Glial-Neuronal Interactions, Riverside, California 92521

Abstract. We present an approach for rapidly and quantitatively mapping tissue absorption and scattering spectra in a wide-field, noncontact imaging geometry by combining multifrequency spatial frequency domain imaging (SFDI) with a computed-tomography imaging spectrometer (CTIS). SFDI overcomes the need to spatially scan a source, and is based on the projection and analysis of periodic structured illumination patterns. CTIS provides a throughput advantage by simultaneously diffracting multiple spectral images onto a single CCD chip to gather spectra at every pixel of the image, thus providing spatial and spectral information in a single snapshot. The spatial-spectral data set was acquired 30 times faster than with our wavelength-scanning liquid crystal tunable filter camera, even though it is not yet optimized for speed. Here we demonstrate that the combined SFDI-CTIS is capable of rapid, multispectral imaging of tissue absorption and scattering in a noncontact, nonscanning platform. The combined system was validated for 36 wavelengths between 650–1000 nm in tissue simulating phantoms over a range of tissue-like absorption and scattering properties. The average percent error for the range of absorption coefficients (μ_a) was less than 10% from 650–800 nm, and less than 20% from 800–1000 nm. The average percent error in reduced scattering coefficients (μ_s') was less than 5% from 650–700 nm and less than 3% from 700–1000 nm. The SFDI-CTIS platform was applied to a mouse model of brain injury in order to demonstrate the utility of this approach in characterizing spatially and spectrally varying tissue optical properties. © *2011 Society of Photo-Optical Instrumentation Engineers (SPIE).* [DOI: 10.1117/1.3528628]

Keywords: spectrometry; brain imaging; absorption; scattering; optical properties; intrinsic signal.

Paper 10299SSR received Jan. 1, 2010; revised manuscript received Oct. 20, 2010; accepted for publication Nov. 29, 2010; published online Jan. 28, 2011.

1 Introduction

Most current techniques for quantifying tissue absorption and scattering are limited in the number of spatial and spectral measurements that can be obtained simultaneously. Optical methods that quantitatively separate absorption from scattering in turbid media are typically based on strategies that employ spatially and/or temporally modulated light sources.[1,2] Both spatial and temporal modulation methods employ either real- or frequency-domain measurements in conjunction with model-based analyses. Most of these methods determine spatially averaged absorption and scattering values in tissue volumes near source and detector optical fibers placed in contact with the tissue, limiting the mapping capability of these techniques to one or a series of discrete measurement locations. One strategy that overcomes the limits to spatial mapping employs the spatial frequency domain and is based on the projection and analysis of periodic structured illumination patterns.[3] This structured or modulated light imaging effectively expands the number sources and detectors to be nearly continuous across the field of view, with a point measurement at each pixel of the camera used. The importance of this approach is its ability to spatially map tissue optical properties, eliminating the need to scan through space when rich spatial data is required. This technology has been shown to map tissue optical properties, have depth-sectioning sensitivity,[3] to recover optical properties from layered structures,[4] and has been used in a number of *in vivo* applications including monitoring hemodynamics during stroke in the brain and in breast tumors.[5–7]

In order to rapidly gather spatial and broadband spectral information simultaneously, we have combined spatial frequency domain imaging (SFDI) with a computed tomography imaging spectrometer (CTIS). SFDI eliminates spatial scanning while CTIS eliminates spectral scanning by taking hyperspectral snapshots,[8] allowing us to reconstruct 156 × 116 pixel images at up to 96 wavelengths (we reconstruct 36 wavelengths here) in each snapshot. This greatly improves measurement speed compared with scanning based hyperspectral methods, such as a liquid crystal tunable filter (LCTF), acousto-optic tunable filter

*Current affiliation: Massachusetts Institute of Technology, G. R. Harrison Spectroscopy Laboratory, 77 Massachusetts Avenue, 6-205, Cambridge, Massachusetts 02139.

Address all correspondence to: Bruce J. Tromberg, University of California, Irvine, Beckman Laser Institute, 1002 Health Science Rd E., Irvine, CA 92612. Tel: 949-824-8705; Fax: 949-824-5413; E-mail: bjtrombe@uci.edu.
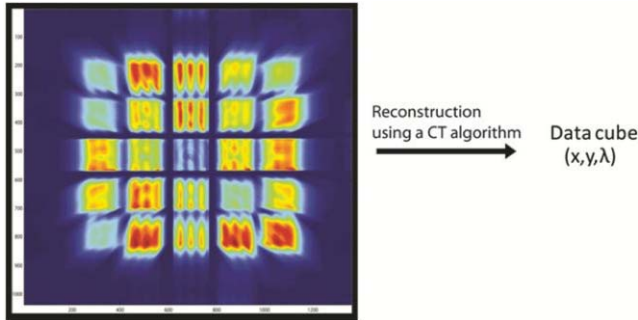
Fig. 1 A raw CTIS snapshot. The center rectangle is the undiffracted image, surrounded by the diffracted orders of the image after it passes through the 2D grating. The snapshot is passed through a computed-tomography (CT) algorithm to produce a data cube of images (x,y) at each desired wavelength.

Fig. 2 Combined structured illumination and CTIS system.

(AOTF), push broom imaging spectrometers or filter wheels, which require separate snapshots for each wavelength. Here acquisition of the spatial and spectral data set was approximately 30 times faster on the same sample with the CTIS than with our LCTF (Nuance, CRI).

Validation of the combined system was performed by measuring a range of tissue phantoms with known absorption and scattering values. The validated SFDI-CTIS system's spatial and spectral resolution of optical properties is demonstrated in a mouse model of brain injury. From the absorption spectra, we recover maps of oxy- and deoxy-hemoglobin, oxygen saturation, total hemoglobin concentration, and water content. We find that the total hemoglobin concentration measured at the site of injury reflects expected literature values for hemoglobin concentration in mouse blood. The water content map shows possible edema in and surrounding the site of visually apparent injury and also corresponds well to an area of decreased μ_s' at all wavelengths. These parameters are clinically useful for monitoring oxygen and hemoglobin delivery to different parts of the brain, and have potential for directly quantifying injury-induced swelling and edema.

2 Materials and Methods

2.1 Instrument

A common implementation of multi-spectral SFDI uses a broadband light source, e.g. quartz tungsten halogen lamp, with filters placed in front of the CCD camera to scan through multiple wavelengths. We typically employ a liquid crystal tunable filter (Nuance, CRI, Woburn, MA) to acquire 36 spectral images between 650–1000 nm with 10-nm spacing, which, depending on the subject, may require tens of seconds per frame. In order to eliminate the time required to scan through wavelength space, we have combined the structured light projection system with a Computed-Tomography Imaging Spectrometer (CTIS), from the Jet Propulsion Laboratory (JPL), NASA.[8] CTIS devices have previously been used in multispectral imaging of the retina.[9] The CTIS used here gives a three-dimensional data cube with 152×116 pixels of spatial information at up to 96 wavelengths in each snapshot. Note that 36 wavelengths are reconstructed in this work, which provides sufficient wavelength information for our application and allows us to compare directly to the range of the LCTF. Fewer wavelengths in the CTIS reconstruc-
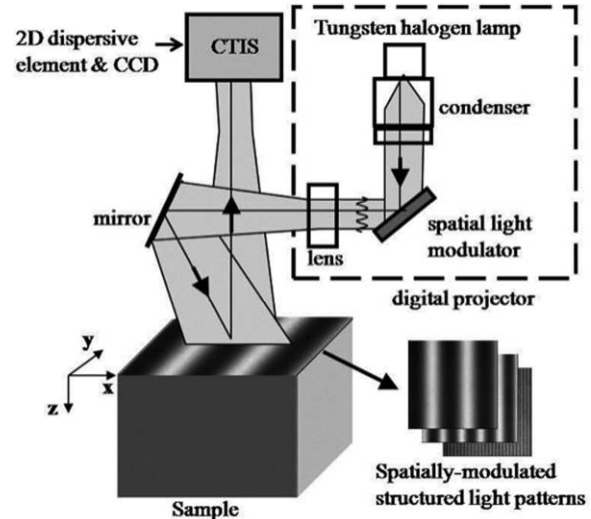
tion also improves signal to noise. The enabling component is a two-dimensional computer generated holographic grating that separates each image into orders of diffraction, as shown in Fig. 1. Note that the application here is not light limited and that our data show sufficient signal even after the diffraction of the image across the CCD. Further analysis of signal to noise for the CTIS can be found in the literature.[10]

These orders are then reconstructed using a computed tomography algorithm into a data cube of images (x, y) at each spectral channel (z). The CTIS instrument can reconstruct wavelength data between 620–1000 nm with 5-nm-wide bands. The strength of the CTIS is that it is a true snapshot spectrometer and can cover the entire spectrum quickly at relatively low cost. The integration time required for one frame in tissue for this work was typically around 500–600 ms. Note here that this CTIS was not designed specifically for tissue measurements and could have shorter integration times with further sensor optimization, and utilization of a brighter, better matched light source. In addition, the grating efficiency of the CTIS can be tailored to the illumination spectrum. Nonetheless, this exposure time greatly decreases the measurement time, by about 30 times compared with LCTF based cameras currently used with structured illumination for equivalent measurement parameters. The combination of these technologies expands the spatial and spectral resolution of diffuse optical measurements to be nearly continuous over the imaged area and near infrared wavelength range.

The combined structured illumination and CTIS platform appears in Fig. 2. Broadband, near infrared light is produced by the quartz tungsten halogen lamp. The lamp is a 250 W, power adjustable source (Newport Oriel, Irvine, CA, model 66883) with a flux controller unit to stabilize the power output of the bulb over time (Newport Oriel, Irvine, CA, model 68950). The light is focused onto a spatial light modulator, in this case, a digital micromirror device (DMD). The DMD, 1024×768 binary mirrors, based on the DLP[TM] technology (Texas Instruments, Dallas, TX), produces the spatially modulated patterns. Here we use temporal averaging over at least 30 ms (simply setting exposure times to be greater than 30 ms) to produce grayscale sinusoidal projections from the binary light/dark positions of the mirrors. A mirror is placed after the projection optics to

direct the projected patterns onto the sample. Images are then gathered through collection lenses into the CTIS. The field of view is variable and dependent on the projection and collection lenses chosen, in this case on the order of 1–2 cm. Crossed linear polarizers at the projector and collection lenses eliminate specular reflection from surface of the sample.

This first implementation of the combined structured illumination and CTIS platform can acquire data at a rate of about 10 frames per minute, which is currently limited by the Labview acquisition rather than the exposure time of the CTIS camera. Note that an equivalent measurement with our LCTF system (Nuance, CRI, Woburn, MA) has a rate of about 0.33 frames per minute. With future software development, such as triggering of the camera at each projection, this could theoretically be increased to around 20 frames per minute (dependent only on the exposure time of the CTIS). Brighter light sources and potential use of fewer spatial frequency phase projections could further contribute to an increased frame rate. The ultimate limits for exposure time here are the albedo of the scene and the ∼30 ms per projection required to produce stable grayscale images with the DMD.

Reconstruction of the CTIS snapshots using the standard CTIS computed tomography algorithm currently takes around 30 seconds per snapshot using a dual-core processor (Intel® Core™ 2 Duo 2.40 GHz) and is currently done after data acquisition. By using both cores of the processor, around 4 snapshots per minute can be reconstructed. The use of multiple core computers, clusters of computers or parallel processing with graphics processing units could speed up the reconstruction of a large number of snapshots.

Another advantage of the combined system is the impact of the projected spatial frequencies on the CTIS reconstructions. It has been shown that adding spatial frequency to the collected images helps to fill in the "missing cone," which is interpreted as a region in spatial-spectral frequency space along the spectral frequency axis where no information is gathered by the CTIS.[11]

2.2 Tissue simulating phantoms

To validate the accuracy of the combined system, titrations of absorption and scattering were performed with ranges of optical properties typical of tissue values. Liquid phantoms were constructed with known concentrations of an absorber (water soluble nigrosin) and scatterer (Liposyn II, a lipid emulsion). Nigrosin absorption was characterized in a spectrometer. Dilutions were made from a stock solution of 250 mg/500 ml of water soluble nigrosin. A 100th dilution of the stock solution results in an absorption coefficient of 0.016 mm^{-1} at 650 nm. Reduced scattering of the lipid emulsion has previously been characterized.[12] In the first set of phantoms, the reduced scattering was increased incrementally between 0.56–1.39 mm^{-1} at 650 nm, while absorption was held constant at 0.0056 mm^{-1}. In the next set of phantoms, the amount of absorber was increased incrementally to give absorption values from 0.0056–0.027 mm^{-1} at 650 nm, while holding the reduced scattering at a constant value of 0.56 mm^{-1}. Two spatial frequencies (0 lines/mm, or unstructured illumination, and 0.29 lines/mm) were used. The calibration phantom for the reduced scattering titration was a separate Liposyn and nigrosin liquid phantom with optical properties at 650 nm that were $\mu'_s = 1.67$ mm^{-1}

and $\mu_a = 0.0056$ mm^{-1}. For the absorption titration the calibration phantom had optical property values at 650 nm of $\mu'_s = 0.97$ mm^{-1} and $\mu_a = 0.01$ mm^{-1}.

2.3 In vivo model

To demonstrate the mapping capabilities and *in vivo* capacity of the combined system, images of a small bleed on mouse cortex were acquired (Under UC Irvine IACUC protocol number 2007-2703). The bleed was caused by a pinprick to exposed dura after craniotomy with a 27 gauge needle. This provided an example with both spectral and spatial inhomogeneities. Two spatial frequencies (0 lines/mm, or unstructured illumination, and 0.27 lines/mm) were used. The measurement took about 5 s to acquire and 3 min to reconstruct and process afterward. The data was calibrated with a silicone tissue phantom of known optical properties.

2.4 Models of light transport for determining tissue optical properties

Current methods of determining tissue optical properties often employ the diffusion approximation to the Boltzmann transport equation.[13] This has been demonstrated for use with structured illumination.[3] Briefly the time independent diffusion equation can be written as:

$$\nabla^2 \varphi - 3\mu_a \mu_{tr}\varphi = -3\mu_{tr}q, \tag{1}$$

where $\mu_{tr} = \mu'_s + \mu_a$, μ_a is the absorption coefficient, μ'_s is the reduced scattering coefficient, φ is the fluence rate, and q is the source term. The source is planar with sinusoidal intensity,

$$q = q_0 \left(\frac{1}{2}\cos(2\pi f_x x + \alpha) + \frac{1}{2} \right), \tag{2}$$

where f_x is spatial frequency (in lines/mm) and α is the spatial phase. Using a fluence rate that varies only with depth (z) in the tissue with the time-independent diffusion equation, we arrive at an equation for fluence that is dependent on the spatial frequency of the source,

$$\frac{d^2}{dz^2}\varphi(z) - \left[3\mu_a\mu_{tr} + (2\pi f_x)^2\right]\varphi(z) = -3\mu_{tr}q_0(z), \tag{3}$$

where we define the parameter μ'_{eff} as

$$\mu'_{eff} = 3\mu_a\mu_{tr} + (2\pi f_x)^2. \tag{4}$$

The inverse of μ'_{eff} is a metric of the average depth of penetration of the light and is both wavelength and spatial frequency dependent. In the near infrared, for typical tissue optical properties, this penetration depth is on the order of several millimeters. Combining this with an extended source, solving for fluence and applying a boundary condition that requires that the flux, j, is proportional to the fluence at the surface, as previously shown, we measure diffuse reflectance, R_d,

$$R_d(k) = \frac{-j|_{z\to 0^+}}{P_0} = \frac{3Aa'}{(\mu'_{eff}/\mu_{tr}+1)(\mu'_{eff}/\mu_{tr}+3A)}, \tag{5}$$

with A as a proportionality constant and a' is the reduced albedo (μ'_s/μ_{tr}).

A summary of the findings of this model shows the impact of spatial frequencies. Low spatial frequencies have the

most sensitivity to changes in absorption, while higher spatial frequencies have sensitivity to scattering changes but greatly reduced sensitivity to absorption. To separate absorption from scattering, a minimum of two spatial frequency projections are needed. Typically one spatial frequency is zero (dc), or planar illumination, and the other is a nonzero (ac) frequency. In order to obtain the entire spatial map of each spatial frequency, each frequency is projected three times, shifting the phase of the sinusoids by 120° and 240° from the original pattern. These three phase images are then "demodulated" for each frequency using the following equation: Reflectance $= 2^{\frac{1}{2}}/3 *[(A - B)^2 + (B - C)^2 + (C - A)^2]$. Note that the demodulation occurs after the CTIS reconstructions are performed. This technique requires a minimum of six spatial frequency projections per measurement: two spatial frequencies with three phase projections each. Once these two spatial frequencies are acquired and demodulated, they are calibrated to a tissue simulating phantom of previously determined optical properties. Using a least-squares nonlinear fit, to minimize the error between the measurement and the model prediction, we arrive at an absorption coefficient, μ_a, and reduced scattering coefficient, μ_s'. We perform this fit at every pixel of the camera.

3 Results and Discussion

3.1 Tissue simulating phantoms

The expected and recovered optical properties for scattering and absorption titrations versus wavelength appear in Figs. 3 and 4, respectively.

The right side of Fig. 3 shows that the scattering titration resulted in recovery of reduced scattering over the range of titrations and wavelengths with an average error of less than ~5%. The left side of Fig. 3 shows the fit for absorption, which was held constant during the scattering titration. Average error for constant absorption was less than 10% from 650–925 nm as

the scattering was varied. Above 925 nm, the error increases. This is explained by the high value of absorption at the water peak (980 nm) compared to the relatively low scattering at these wavelengths. The μ_s'/μ_a ratio in these regions for the two lowest scattering phantoms ranged from 6–11, which begins to challenge the requirement of the diffusion model for scattering to be much greater than absorption. We see that for the two highest scattering phantoms, the μ_s'/μ_a in the >950 nm range is at least 15 and the error decreases significantly. In the wavelength regions of lowest error, $\mu_s'/\mu_a \sim 100$. We also suffer from relatively low light source power and decreased detector sensitivity in this wavelength region, factors that contribute to diminished signal to noise. The left side of Fig. 4 shows that the absorption titration resulted in average errors of less than 10% from 650–800 nm, and less than 20% from 800–1000 nm. The right side of Fig. 4 shows that the reduced scattering value, held constant throughout the absorption variation, fit very well, with an average error of less than 5%. These errors are similar to those previously reported for a spatial frequency domain imaging system at 660 nm using a 660 nm filter and Roper Cascade 512F camera (absorption titration error <15%, scattering titration error <10%, over a slightly different range of optical properties).[14]

3.2 In vivo model

A dc reflectance image of the mouse cortex at 650 nm is shown in Fig. 5, with a region of interest chosen (dashed line) to show the small bleed and surrounding normal brain on the right side of the cortex.

Maps of the resulting absorption and reduced scattering at 650 nm appear in Fig. 6. Each image contains 63×39 pixels, cropped from the full CTIS resolution of 152×116 pixels, to highlight the injured and surrounding areas, and measures 6.49×4.02 mm. In the absorption map, the contrast of the small bleed relative to surrounding brain is very clear. The absorption
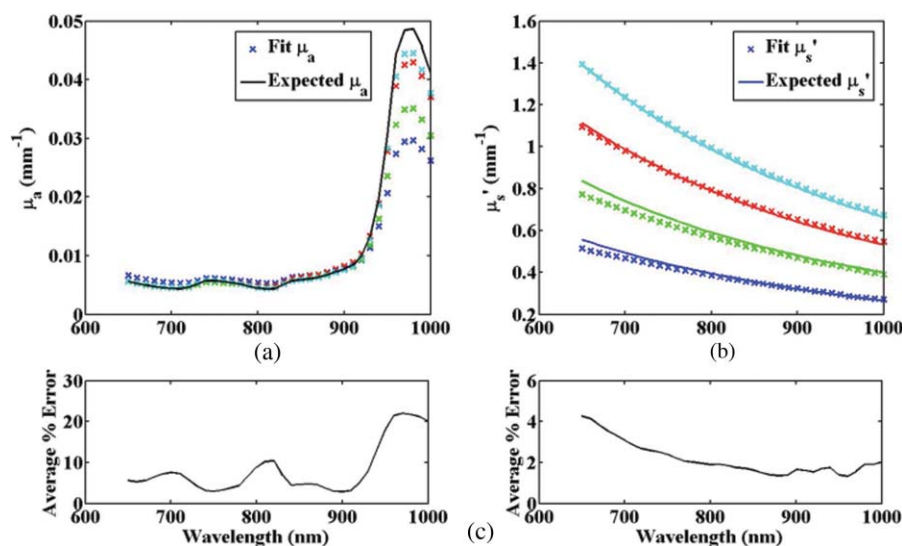

Fig. 3 Scattering titration results. Each color represents a phantom with different concentration of scatterer. Absorption was held constant. X's mark the fit or recovered data points, while solid lines represent the expected values. (a) Fit and expected absorption coefficient versus wavelength, held constant. Colors correspond to the scattering titration phantoms of the same color. (b) Fit and expected reduced scattering coefficient versus wavelength for each of five different scatterer concentrations. (c) The absolute value of the average % error over the range of the titration at each wavelength. Calibration phantom values at 650 nm: $\mu_s' = 1.67$ mm^{-1} and $\mu_a = 0.0056$ mm^{-1}. Number of pixels, n = 10 × 13 (cropped and binned), standard deviation of scattering = <4% at 650 nm.
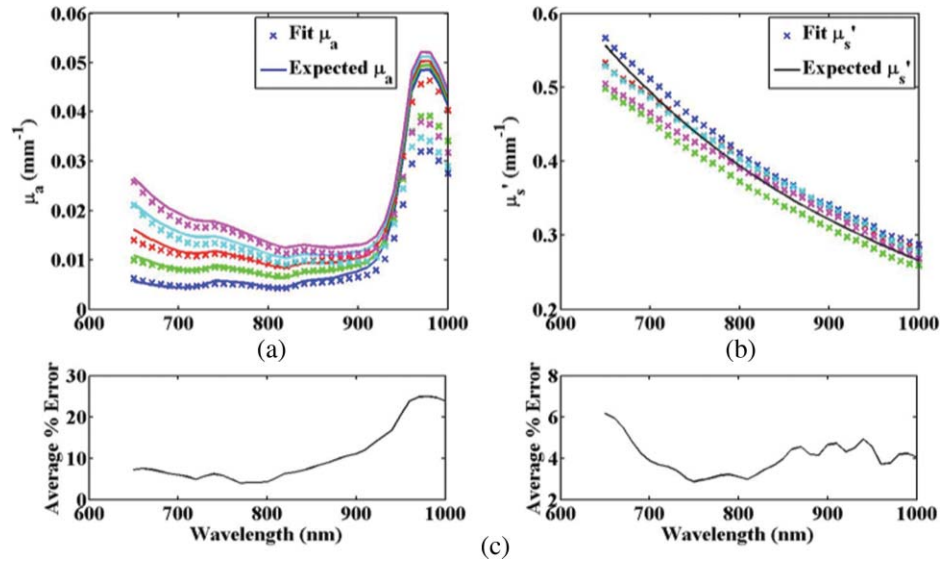
Fig. 4 Absorption titration results. Each color represents a phantom with different concentration of absorber. Scattering was held constant. X's mark the fit or recovered data; solid lines represent the expected values. (a) Fit and expected absorption coefficient versus wavelength for each of five different absorber concentrations. (b) Fit and expected reduced scattering coefficient versus wavelength, held constant. Colors correspond to the absorption titration phantom of the same color. (c) The absolute value of the average % error over the range of the titration at each wavelength appears below the plots. Calibration phantom values at 650 nm: $\mu_s' = 0.97$ mm^{-1} and $\mu_a = 0.01$ mm^{-1}. Number of pixels, n = 10 × 13 (cropped and binned), standard deviation of absorption at 650 nm = <6.5%.

at 650 nm in the bleed is over six times that of the surrounding brain. This contrast is expected due to the strong absorption of hemoglobin at 650 nm. In the reduced scattering map, values are lower in the area of the bleed by about two- to -threefold versus the surrounding tissue. This is also expected, since blood is composed mostly of plasma and therefore, compared to tissue, has a significantly lower density of cellular scattering particles with no comparable extracellular matrix. Note that the overall area of decreased scattering surrounding the bleed is larger than the area of increased absorption. In this experiment, the dura matter was punctured, which may have caused local swelling in addition to the bleed (further discussion appears below).
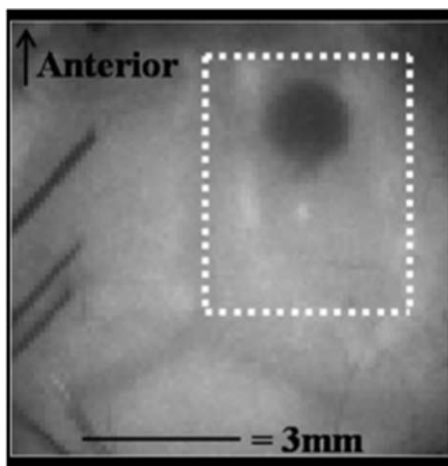

Fig. 5 Mouse cortex with a region of interest (dashed rectangle) chosen to include one side of the cortex containing the site of the small bleed and surrounding normal tissue. The top of the image is the anterior side of the brain.

Figure 7 shows absorption and reduced scattering spectra (650–1000 nm) from two regions of interest (ROIs). The ROIs were selected to highlight differences in physiology: one normal cortical region and one in which a small bleed occurred. The green ROI appears over normal cortex and the blue ROI is over the site of the bleed. The reduced scattering spectra show that scattering is lower in the bleed than in the surrounding brain over the whole wavelength range, which is consistent with less cellularity in blood versus neural tissue, as previously discussed.

The absorption spectra in both ROIs contain features of oxy- and deyoxy- hemoglobin and water.[14] The absorption in the blue ROI over the bleed is higher across the entire wavelength range. This is because the blood, containing mostly hemoglobin and water, accumulates at the bleed. In the area of the bleed, the concentration of total hemoglobin should approach that of whole mouse blood. Calculating the expected concentration of hemoglobin in whole mouse blood from literature values of 10–17g/dL, a hematocrit range of 35–52%,[15] and the molecular weight of hemoglobin as 64.5×10^3 g/mol, we arrive at an expected range of about 543–1371 μM (from: ([10 to 17 g/dL] × [35 to 52% hematocrit] / [64. 5 × 10^3 g/mol]).

Using absorption values from 33 wavelengths in a Beer–Lambert law fit for oxy- and deoxy-hemoglobin and water in the area of the bleed, we calculated a total hemoglobin concentration of about 496 μM at the center of the bleed, and a water percentage of about 80–98% as shown in the chromophore maps in Fig. 8. Given the small size of the bleed (less than ~2 mm in diameter), it is likely that the total hemoglobin concentration falls just below the low end of the expected range due to the measurement sampling some volume of brain below and around the bleed. This "partial volume" effect would result in an averaging of the hemoglobin concentrations of the bleed and a small volume of brain.[16] A map of oxygenation is shown in Fig. 8 (bottom plot, S$_t$O$_2$ map). Further characterization of the
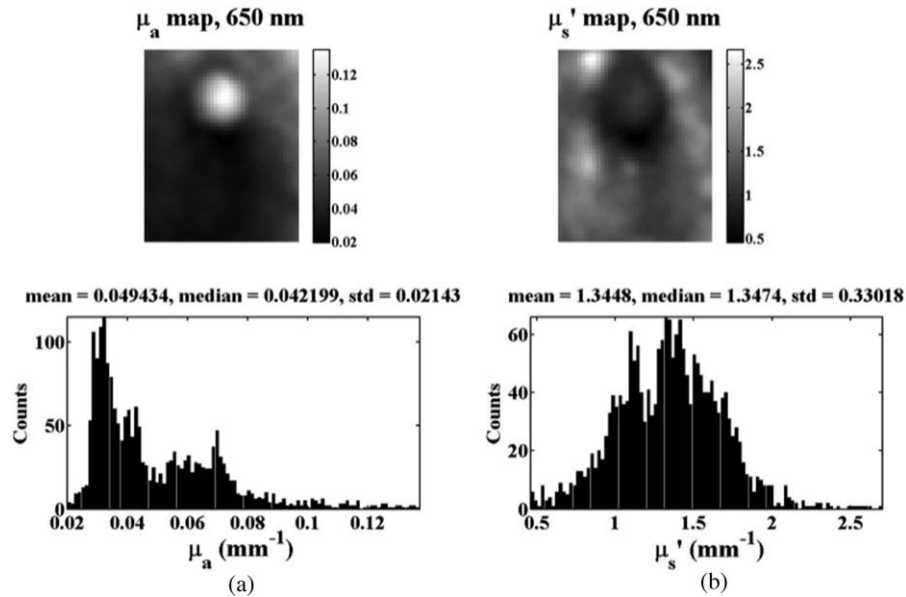
Fig. 6 Optical property maps (top) and histograms (bottom) of mouse cortex at and surrounding the site of injury at 650 nm. (a) Absorption map and (b) reduced scattering map. The image is 6.49 × 4.02 mm, 63 × 39 pixels.

combined system's ability to recover correct tissue oxygenation values can be done using side-by-side tissue oximeter and SFDI-CTIS measurements. This would be a key validation step in the process of developing this technology as an imaging oxygenation monitor. We can see in the water map in Fig. 8 that the shape of the area with higher water concentration is similar to the shape of the reduced scattering map rather than the pattern of increased hemoglobin. This supports the idea that there is local swelling at the location of the bleed. We expect that the presence of both blood and water would decrease tissue scattering by diluting the number-density of scatterers in the field-of-view.

Overall, SFDI and CTIS technologies provide complementary information resulting in rapid acquisition of comprehensive spatial and spectral data. The use of structured illumination separates absorption from scattering at each pixel, while the CTIS gathers multispectral data in each pixel simultaneously. Each technology sacrifices part of its range as a tradeoff to the combination. Image resolution is decreased to the spatial resolution of the undiffracted part of the CTIS image, while the acquisition speed of the CTIS is limited by the number of spatial frequency projections required for each frame of SFDI. Specifically, a CTIS image is roughly 1/5 the number of pixels in a 4 × 4 spatially binned LCTF image using our Nuance camera
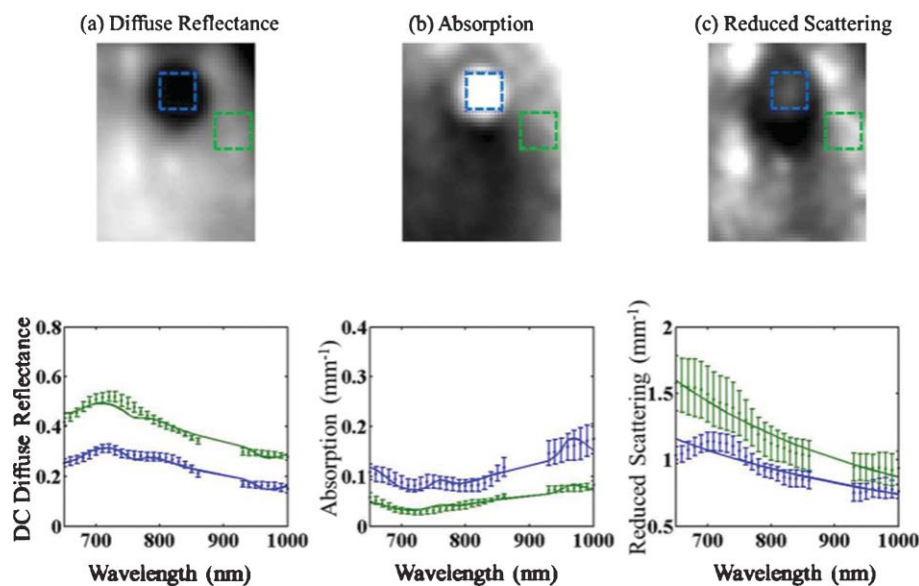

Fig. 7 (a) Diffuse reflectance map of mouse cortex at and surrounding the site of injury at 650 nm, (b) absorption, and (c) reduced scattering maps. Regions of interest detailing the absorption and scattering spectra over normal cortex (green), a small pool of blood (blue). The image is 6.49 × 4.02 mm, 63 × 39 pixels. (Color online only.)
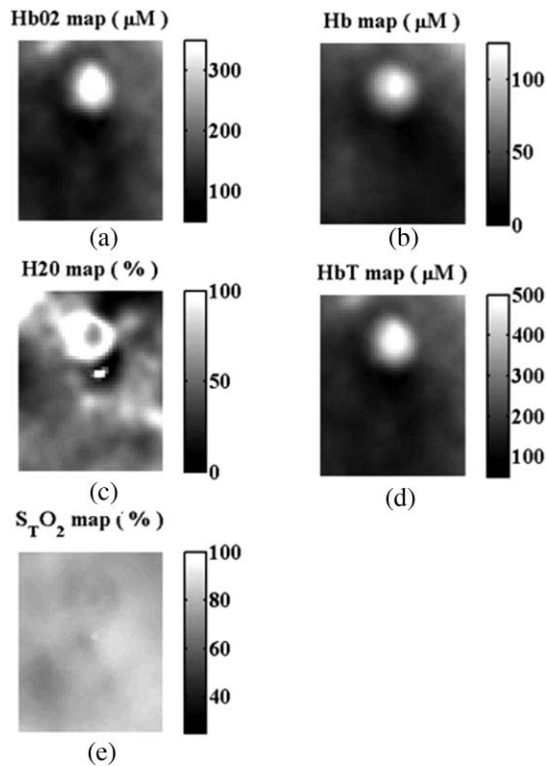
Fig. 8 Chromophore maps for mouse cortex at and surrounding site of injury, fit from the absorption spectra. (a) Oxy-hemoglobin concentration (HbO$_2$), (b) deoxy-hemoglobin concentration (Hb), (c) water percentage (H$_2$O), (d) total hemoglobin concentration (HbT), and (e) oxygen saturation percentage (S$_T$O$_2$). Each image is 6.49 × 4.02 mm, 63 × 39 pixels.

(note that 4 × 4 binning is typically done to shorten exposure times). Though this lower spatial resolution is sufficient for many applications, larger format CTIS devices are being developed to increase spatial resolution. Each CTIS image of tissue only takes ∼200–600 ms, however the ∼6 s temporal resolution of the combined system is limited by the acquisition software and by the six spatial frequency images required to perform SFDI. With faster software, brighter sources, and potentially fewer spatial frequency patterns, the acquisition time of the CTIS-SFDI system could approach less than 1 s. Faster reconstructions are being developed to reduce reconstruction times and bring CTIS closer to near real time analysis.

4 Conclusions

In summary, we have developed and validated a combined platform for fast multispectral mapping and quantitation of optical absorption and scattering. The value of this approach can be high for applications that require mapping of multiple spectrally resolved parameters simultaneously as well as in new or exploratory applications in which the optimal measurement wavelengths need to be determined. Rapid acquisition capabilities are well-suited to dynamic measurements of many chromophores in critical tissues such as brain where assessing tissue status and composition can provide real-time insight into challenging problems of neurophysiology, such as injury progression, treatment response, and measuring cortical activity.

References

1. K. Yoo and R. Alfano, "Determination of the scattering and absorption lengths from the temporal profile of a backscattered pulse," *Opt. Lett.* **15**(5), 276–278 (1990).
2. T. J. Farrell, M. S. Patterson, and B. Wilson, "A diffusion theory model of spatially resolved, steady-state diffuse reflectance for the noninvasive determination of tissue optical properties *in vivo*," *Med. Phys.* **19**(4), 879–88 (1992).
3. D. J. Cuccia, F. Bevilacqua, A. J. Durkin, and B. J. Tromberg, "Modulated imaging: quantitative analysis and tomography of turbid media in the spatial-frequency domain," *Opt. Lett.* **30**(11), 1354–6 (2005).
4. J. R. Weber, D. J. Cuccia, A. J. Durkin, and B. J. Tromberg, "Non-contact imaging of absorption and scattering in layered tissue using spatially modulated structured light," *J. Appl. Phys.* **105**, 102028 (2009).
5. D. J. Cuccia, F. Bevilacqua, A. J. Durkin, F. R. Ayers, and B. J. Tromberg, "Quantitation and mapping of tissue optical properties using modulated imaging," *J. Biomed. Opt.* **14**, 024012 (2009).
6. D. Abookasis, C. C. Lay, M. S. Mathews, M. E. Linskey, R. D. Frostig, and B. J. Tromberg, "Imaging cortical absorption, scattering, and hemodynamic response during ischemic stroke using spatially modulated near-infrared illumination," *J. Biomed. Opt.* **14**, 024033 (2009).
7. A. Moy, J. G. Kim, E. Y. H. P. Lee, B. J. Tromberg, A. Cerussi, and B. Choi, Brca1/p53 Deficient Mouse Breast Tumor Hemodynamics During Hyperoxic Respiratory Challenge Monitored by A Novel Widefield Functional Imaging (WiFI) System, *Proc. SPIE*, **7174**, 71742L (2009).
8. M. R. Descour, C. E. Volin, E. L. Dereniak, K. J. Thome, A. B. Schumacher, D. W. Wilson, and P. D. Maker, "Demonstration of a high-speed nonscanning imaging spectrometer," *Opt. Lett.* **22**, 271–1273 (1997).
9. W. R. Johnson, D. W. Wilson, W. Fink, M. Humayun, and G. Bearman, "Snapshot hyperspectral imaging in ophthalmology," *J. Biomed. Opt.* **12**(1), 014036 (2007).
10. C. E. Volin, M. R. Descour, and E. L. Dereniak, "Signal-to-noise ratio analysis of the computed-tomography imaging spectrometer," *Proc. SPIE* **3438**, 107 (1998).
11. W. R. Johnson, D. W. Wilson, and G. Bearman, "Spatial-Spectral Modulating Snapshot Hyperspectral Imager," *Appl. Opt.* **45**, 1898–1908 (2006).
12. H. van Staveren, C. J. M. Moes, J. van Marie, S. A. Prahl, and M. J. C. van Gemert, "Light scattering in Intralipid-10% in the wavelength range of 400–1100 nm," *Appl. Opt.* **30**, 4507–4514 (1991).
13. A. Ishimaru, *Wave Propagation and Scattering in Random Media*, IEEE Press, New York (1978).
14. B. J. Tromberg, N. Shah, R. Lanning, A. Cerussi, J. Espinoza, T. Pham, L. Svaasand, and J. Butler, "Non-invasive *in vivo* characterization of breast tumors using photon migration spectroscopy," *Neoplasia* **2**(1), 26–40 (2000).
15. J. G. Fox, *The Mouse in Biomedical Research*, Edition 2, Elsevier, Amsterdam (2007).
16. T. Durduran, G. Yu, M. G. Burnett, J. A. Detre, J. H. Greenberg, J. Wang, C. Zhou, and A. G. Yodh, "Diffuse optical measurement of blood flow, blood oxygenation and metabolism in a human brain during sensorimotor cortex activation," *Opt. Lett.* **29**, 1766–1768 (2004).